LA-UR 91 252

LA-UR--91-252

DE91 007470

Los Alamos National Laboratory is operated by the University of California for the United States Department of Energy under contract W-7405-ENG-36

TITLE A Phenomenological Model of Thermal-Hydraulics of Convective Boiling During the Quenching of Hot Rod Bundles; Part II: Assessment of the Model with Steady-State and Transient Post-CHf Data

AUTHOR(S) Cetin Unal
Ralph A. Nelson

SUBMITTED TO 1991 National Heat Transfer Conference
July 28-31, 1991
Minneapolis, Minnesota

DISCLAIMER

Los Alamos National Laboratory
Los Alamos, New Mexico 87545

FORM NO. 836 R4
ST. NO. 2629 5/81

A PHENOMENOLOGICAL MODEL OF THERMAL-HYDRAULICS OF CONVECTIVE BOILING DURING THE QUENCHING OF HOT ROD BUNDLES; PART II: ASSESSMENT OF THE MODEL WITH STEADY-STATE AND TRANSIENT POST-CHF DATA

by

Cetin Unal and Ralph Nelson

Los Alamos National Laboratory
Nuclear Technology and Engineering Division
Engineering and Safety Analysis Group
Los Alamos, NM 87545

ABSTRACT

After completion of the thermal-hydraulic model developed in a companion paper, we performed developmental assessment calculations of the model using steady-state and transient post-critical heat flux (CHF) data. This paper discusses the results of those calculations.

The overall interfacial drag model predicted reasonable drag coefficients for both the nucleate boiling and the inverted annular flow (IAF) regimes. The predicted pressure drops agreed reasonably well with the measured data of two transient experiments, CCTF Run 14 and a Lehigh reflood test. The thermal-hydraulic model for post-CHF convective heat transfer predicted the rewetting velocities reasonably well for both experiments. The predicted average slope of the wall temperature traces for these tests showed reasonable agreement with the measured data, indicating that the transient-calculated precursory cooling rates agreed with measured data.

The hot-patch model, in conjunction with the other thermal-hydraulic models, was capable of modeling the Winfrith post-CHF hot-patch experiments. The hot-patch model kept the wall temperatures at the specified levels in the hot-patch regions and did not allow any quench-front propagation from either the bottom or the top of the test section. The interfacial heat-transfer model tended to slightly under-predict the vapor temperatures. The maximum difference between calculated and measured vapor temperatures was 20%, with a 10% difference for the remainder of the runs considered. The wall-to-fluid

heat transfer was predicted reasonably well, and the predicted wall temperatures were in reasonable agreement with measured data with a maximum relative error of less than 13%.

I. INTRODUCTION

As pointed out in a companion paper (1), a significant number of experimental and analytical studies reporting on post-critical heat flux (CHF) boiling and quenching have been published in the last two decades. However, a large amount of scatter still exists between the predictions from published correlations and measured data (2). This disagreement between the models and data was attributed to the fact that the hydraulic and heat-transfer models typically are developed independent of one another and, when combined, produce a large part of the scatter. Thus, even when "the best heat transfer and hydraulic models" are combined and compared with either the original data sets or new ones, significant scatter is not surprising. To develop more accurate models, information on heat transfer must be integrated with the best available hydrodynamic data in the model development process. Ultimately, any experiment that measures all the required quantities is needed; however, the state-of-the-art in measurements is not capable yet of doing such an experiment.

The problem of "integrated model development" is compounded in two-phase two-fluid thermal-hydraulic computer codes, such as TRAC, that solve the mass, momentum, and energy equations for each phase. To accomplish this solution, they require closure relationships to determine mass, momentum, and heat-transfer interchange between the phases and between both heated or unheated structures and the phases. Because phasic closure relationships are generally not available, code developers are forced to infer these phasic relationships based on limited information available from the data they are analyzing. This frequently is done by modifying existing models and combining these modified models to represent the different phenomena for the required phasic contributions. This process has received much debate.

During the development of the reflood model, our approach to defining these phasic closure relationships was to use correlations known to apply to a given regime for a particular closure quantity wherever possible. However, the original

correlation frequently could not be applied directly but had to be modified. For those cases, we tried to use the "kernel or functional dependence" of the original correlation and modify only its magnitude by use of a multiplier. This assumes the original model developer was able to capture and represent the functional dependence of the controlling physical quantities. When no correlations were available for given regimes, we tried to define known bounding regimes and use a weighting function between the known regimes to represent the unknown quantities. This assumes the process is continuous and bounded between the two known regimes. In two instances for wall heat transfer, we had to develop separate models to represent the phenomena—the models for transition boiling and the near-wall-liquid post-CHF film boiling effect. The overall model, which is discussed in the companion paper (1), was implemented into the TRAC-PF1/MOD2 computer code.

This paper will discuss the adjustment process of the modifying constants and weighting factors, which we will call "empirical constants." We then will apply the resulting model to a limited number of experimental results to provide some limited assessment of the model.

The adjustment of the empirical constants involved several iterations. Briefly, the empirical constants for the interfacial drag model were found using a reasonable set of coefficients for the wall heat transfer and CCTF Run 14 (3). Then, fine adjustment and correlation of the near-wall-liquid post-CHF film boiling effect were done for the wall and interfacial heat transfer using a set of six Winfrith steady-state post-CHF hot-patch runs (4). After implementation of the adjusted and correlated heat-transfer coefficients, the interfacial drag model again was checked and readjusted as needed with the CCTF Run 14 pressure drop data. The last step involved evaluating the B-coefficient used in the transition boiling model (see Ref. 1). The B-coefficient was determined in such a way that the predicted and measured quench front propagation rates were reasonable in CCTF Run 14 and Lehigh rod bundle (5) tests.

The adjustment of the empirical constants used in the interfacial drag models could best be done using steady-state experimental data obtained for each individual regime. However, such data are not yet available in the literature for the inverted annular flow (IAF) regimes. The data we used in the development of the drag model is the transient quasi-steady pressure drop data obtained for CCTF Run 14. During a reflood test, any particular elevation in the test section experiences dispersed, agitate, rough-wavy IAF, smooth IAF, transition boiling, and finally nucleate boiling. Although the presence of these regimes is not measured directly, the

amount of liquid that occurs between any two elevations is indicated by the pressure drop between them. Thus, between any two particular elevations (the distance between the pressure taps) where a known flow regime exists over a given time window, the pressure drop data can be used to determine the necessary empirical constants.

We adjusted the empirical constants described in interfacial drag models (see Ref. 1) by reasonably matching the pressure drop data in this time-window-by-window method. The problem that makes this adjustment somewhat complicated is that the pressure taps are spaced far enough apart (about 0.6 m) that multiple regimes occur between them. The only regimes that occur uniquely between the ports are nucleate boiling, dispersed flow, and perhaps the post-agitated regime. Thus, one can not determine the necessary empirical constants uniquely for smooth IAF, rough-wavy IAF, and agitated IAF. We can see only the spatial integrated effect, which typically includes these regimes plus one of the other regimes.

This drag adjustment process is cumbersome because of the hydraulic feedback that occurs between the drag flow regimes. Fortunately, although the heat transfer and drag are coupled, they are not tightly coupled, which allows for separate adjustment steps. This drag feedback effect can be minimized by working the problem from bottom up, i.e., nucleate boiling through film boiling. Although the technique yields reasonable results, as noted above, it is not possible to match pressured drop data in all of the flow regimes simultaneously. Section II.A will discuss the results obtained for the pressure drop predictions of CCTF Run 14 and Lehigh rod bundle tests.

To adjust the empirical constants associated with the wall and interfacial heat-transfer models, a limited set of Winfrith steady-state post-CHF hot-patch tests (Runs 149, 177, 122, 104, 98, and 157) was used. Five of the six selected tests were performed at 2 bar, a nearly constant heat flux range of 4.0 to 4.6 W/cm^2, and inlet temperatures of 115 to 116°C, but different inlet mass fluxes ranging from 48 to 1007 kg/m^2s, were used. The last test included higher pressure and heat flux conditions. Assessment of the final model, with nine other Winfrith post-CHF tests having different operating conditions, is presented in Sec. II.C. This assessment compares only the calculated and measured wall and vapor temperatures because no pressure drop data were available for these tests. However, for Run 176, the spatial integral effect of the calculated drag coefficients and void fractions are compared indirectly using the inferred actual quality at the end of the test section.

In the absence of steady-state data without the influence of hot-patches, it is difficult to determine the B-coefficient required by the transition boiling model (see Ref. 1) and that controls the rate of the quench-front propagation. The B-coefficient was adjusted by matching the experimental quench-front velocity of CCTF Run 14 and the Lehigh rod bundle test. The Capillary and vapor Reynolds numbers at the CHF point, which control the selection of the B-coefficient, vary significantly during these transient calculations. The initial results in predicting the quench-front propagation in CCTF Run 14 and Lehigh tests indicated that two different proportionality constants were needed to match the experimental data. The CCTF Run 14 test included flow conditions with relatively high vapor Reynolds number (time-average value), indicating the vapor flow was mostly turbulent. The time-averaged Reynolds number in the Lehigh test was less than 2000, indicating the vapor flow was laminar during the transient. Thus, the B-coefficient was assumed to be 16 for a vapor Reynolds number less than 2000 and 10 for a vapor Reynolds number higher than 2000. We discuss the results for the quench-front propagation rates obtained from this model with the CCTF Run 14 and Lehigh tests in Sec. II.C. Because the characteristics of the tests were used in coefficient definition, this comparison cannot be called an "independent assessment."

II. DISCUSSION OF RESULTS AND COMPARISON

The description of the each test selected for this assessment work, the experimental test procedure, and the TRAC input models are not discussed in this paper. They are available in Ref. 6. The results and lessons learned from the assessment of the final model with transient and steady-state data are discussed below.

A. The Predicted Pressure Drop Histories

The predicted and measured pressure drops between axial locations of 0.0 to 0.61 m (distances refer to the core inlet and are written as 0.0–0.61 m in the remainder of the paper) and 0.61–1.22 m for CCTF Run 14 are shown in Fig. 1. The solid lines show the predicted pressure drop history, whereas the measured data are shown with dotted lines. Subcooled liquid begins flowing into the core bottom at 68 s into the transient. As soon as this liquid flow begins, the predicted pressure drops increased and, correspondingly, the void fractions in the core decreased sharply, as shown in Figs. 1 and 2. Figure 2 shows the predicted void fractions in

Cells 2–7, which determine the pressure drops over the two regions. This fast transient continues a few seconds, after which the void fractions level off.

The pressure drop between axial elevations of 0.0–0.61 m (in cells 2–4) was under-predicted by about 500 Pa until 105 s, as shown in Fig. 1. At about 105 s, the quench front leaves Cell 4. After 105 s, Cells 2–4 have all been quenched and are experiencing nucleate boiling. The second cell was filled by water, whereas the third and fourth cells are in two-phase nucleate boiling (see Fig. 2). The predicted pressure drop between 0–0.61 m was in reasonable agreement with the measured data. The time window from about 105 to 400 s indicates that the interfacial drag coefficient (IFDC) model for the subcooled and low-void nucleate boiling region predicts reasonable IFDCs Therefore, the under-prediction of the pressure drop between 68 and 105 s indicates that the interfacial drag coefficients in inverted annular flow regimes in the low-void fraction region (see Fig. 4 in Ref. 1) are slightly over-predicted, causing the over-prediction of the void fraction in Cell 4. As shown in Fig. 2, the second cell was filled by the water right after the injection was activated. The void fraction in the third and fourth cells varies between 10% to 40% in the time window of 68–105 s, when these cells were experiencing IAFs (smooth, rough-wavy, and agitated IAFs).

The pressure drop upstream of the mid-plane of the core (0.61–1.22 m) is in reasonable agreement with measured values. The quench front leaves Cell 7 at about 215 s, and Cells 5–7 (located between the axial elevations of 0.61 and 1.22 m) are all in nucleate boiling. After 215 s, the average void fraction in Cells 5–7 is about 0.4 but increasing with elevation. The pressure drop is slightly over-predicted. This implies that the void nucleate boiling interfacial drag model slightly under-predicts the IFDCs for these slightly higher voids. The interfacial drag model performs an interpolation to determine the IFDC in the void fraction range of 0.5–0.98, so this interpolation has begun for only cell 7. As the quench front enters cell 5, the predicted void fractions in Cells 5–7 range from 0.4 to 0.8, and the flow regime in these cells is mostly post-agitated IAF. The prediction is oscillatory before 105 s, where the quench front enters cell 5, but the IFDCs are again slightly over-predicted after this time for the IAF flow regimes.

Near the mid-plane of the core (1.22–1.83 m), agreement between the calculated and measured data is reasonable (see Fig. 3), although some oscillations are evident. After 365 s, Cells 8–10 are all experiencing nucleate boiling. Thus, the prediction of the IFDC's in the higher void nucleate boiling region has improved because the predicted pressure drop between 1.22–1.83 m is in good agreement with

the measured data (see Fig. 3). However, in the time window preceding the quench of these levels, the IFDCs are again slightly over-predicted in the post-agitated regime, resulting in an under-prediction of the pressure drop by 150 to 500 Pa (an estimated average of about 250 Pa).

Downstream of the mid plane (1.83–2.44), the under-prediction becomes more noticeable (see Fig. 3) before the quench front nears that level at about 350 s. In terms of absolute pressure drop, this is still within 250 Pa. Although not shown, this same characteristic also is seen at the higher levels in the core. These differences will be discussed in greater detail later.

For now, it can be concluded that predictions of low and high void nucleate boiling IFDCs were reasonable, whereas intermediate void nucleate boiling IFDCs were slightly over-predicted. However, the over-prediction was not significantly high (about 400 Pa) and decreased with increasing void fraction. The IFDCs for IAFs were slightly under-predicted at lower void fractions and over-predicted at higher void fractions. They were in reasonable agreement with the measured data in the intermediate void fraction region. In the CCTF run, the IAF for low voids mostly consists of agitated and post-agitated IAFs. The IFDC in agitated IAF is expected to increase when compared with smooth and rough-wavy IAFs. This increase is not considered in the current model, and the IFDC is calculated using the rough-wavy IAF IFDC model. Thus, the predicted IFDCs in agitated and correspondingly post-agitated IAFs are relatively low. When the IAF flows occur with high void, the IFDCs are calculated using the highly dispersed IFDC model. The reason for the over-prediction of IFDCs in highly dispersed flow is discussed below.

To better understand the disagreement at the upper elevations of the core, it is necessary to note that the highly dispersed IAF interfacial drag model consisted of two components. The IFDC model for liquid droplets and the IFDC model for the liquid film on the unheated surfaces. We have adjusted necessary coefficients to partition the total pressure drop in such a way that the liquid droplet contribution agrees with data available in the Lehigh rod bundle test that had no unheated surfaces and then tried to adjust the cold-wall film effect using the CCTF Run 14 data.

The predicted pressure drop trace between 0.406–0.609 m for the Lehigh run is shown in Fig. 4. The measured pressure drop data in the time window of 25–100 s also is marked in the figure. Only the average value with an uncertainty range is shown in Fig. 4. The predicted and measured values agree reasonably with each other. This indicates that the highly dispersed IFDC model predicts the droplet contribution correctly. Thus, the differences between the calculated and measured

pressure drops downstream of the mid-plane of the core in CCTF run are attributed to the modeling of the unheated wall liquid film contribution.

Comparison of the IFDCs determined by the unheated wet-wall model and its relationship to those for the droplets showed proper trends, i.e., the drag coefficient for the film was much reduced over that of the droplets. However, this reduction was not enough based on current estimates of the partitioning of how much of this higher void liquid was on the wall and how much was in the form of droplets. With the current TRAC two-field formulation, it is difficult to represent the cold-wall effect accurately. In fact, one conceptually ends up levitating liquid with the vapor flow instead of suspending liquid on a surface as actually is required. In practice, with a transient such as CCTF Run 14, one most likely would end up oscillating the two-phase flow around the mean value desired. Although this approach may work for some ranges of void fractions, the correct prediction of the unheated wall contribution requires another field for the liquid film.

B. Post-CHF Heat Transfer with Winfrith Steady-State Post-CHF Data

This section discusses the adjustment and assessment of the post-CHF film boiling model using Winfrith steady-state hot-patch experiments. Section II.A.1 discusses the adjustment of the film boiling model using six tests. Section II.B.2 discusses the results obtained from the hot-patch model. Finally, in Sec. II.B.3, the adjusted model was assessed against nine other Winfrith steady-state post-CHF tests.

1. Adjustment of the Post-CHF Heat Transfer with Winfrith Steady-State Post-CHF Data. The weighting factors and constants for the wall-to-fluid and interfacial heat transfer were adjusted by predicting the measured wall and vapor temperatures for six selected Winfrith post-CHF tests. The operating parameters for these selected runs listed below.

Run No.	G kg/m^2s	P Bar	q W/cm^2	T_{in} °C
149	48	2.02	4.14	115.7
177	103	2.01	4.51	115.6
122	201	2.02	4.68	116.2
104	505	2.02	4.67	115.3
98	1007	2.02	4.89	115.8
157	102	10.0	9.09	177.4

The mass flux was varied; the heat flux, pressure, and inlet subcooling were kept constant for Runs 149, 177, 122, 104, and 98. For each of these five tests, a fixed empirical coefficient used in the near-wall liquid model was determined by matching experimental wall and vapor temperature profiles with the calculated values as close as possible. Next, these coefficients were correlated in terms of the vapor Reynolds number defined at the beginning of the agitated IAF for each of the runs.

Run 157 was used to determine the effect of pressure on the correlated near-wall wall-to-liquid heat transfer. To predict the measured wall and vapor temperatures in this high-pressure run, the vapor Reynolds number dependent constant required a decrease. Therefore, we introduced an exponent to the vapor Reynolds number.

The predicted and measured wall and vapor temperature profiles for these six tests are summarized in Figs. 5 and 6 and show reasonable agreement. In these calculations, the wall-to-vapor heat-transfer coefficient (HTC) calculated by the Webb-Chen correlation was increased 20% to predict the experimental wall and vapor temperatures at the end of the test section.

2. Assessment of the Hot-Patch Model with Winfrith Steady-State Post-CHF Data. One major difficulty in conducting steady-state post-CHF experiments is preventing propagation of the quench front into the test section. Using the hot-patch technique (6) allows researchers to create stabilized post-CHF conditions throughout the test section. A hot-patch model was developed as a feature of the slab heat structure component in TRAC computer program (6). The axial elevations of the hot-patch inlet and outlet and hot-patch temperatures are input parameters to this model. The hot-patch model uses a very high convective-heat-transfer coefficient on the outer surface of the slab to simulate an imaginary heat source at the specified hot-patch temperature. Thus, the necessary energy to prevent the quench-front propagation could be provided by this heat source. The boundary conditions at the inner surface of the slab in the test section are determined by the convective post-CHF conditions. This assessment work modeled both the lower and upper hot patches used in Winfrith steady-state post-CHF tests.

All calculations discussed in this paper were performed in a transient mode. A snap-shot of the transient calculation when thermal-hydraulic conditions had stabilized was analyzed and compared with the steady-state data. The calculated wall surface temperature histories at eight different axial elevations are shown in Fig. 7 for Run 176 to illustrate that the solution had converged. The locations of the inlet

and outlet of the lower and upper hot patches are 0.16, 0.2, 1.12, and 1.256 m, respectively. The wall surface temperatures do not change after 100 s, indicating a converged solution and that steady-state post-CHF conditions at each elevation were obtained. The quench front is located 2.6 mm upstream of the lower hot patch. The wall temperature for the inside of the tube at the beginning of the lower hot patch is 746 K, less than the specified hot-patch temperature of 875 K. However, 1 cm downstream of the hot-patch inlet, the calculated hot-patch surface temperature is calculated to be 864 K, indicating that the quench front is held at the beginning of the lower hot patch. The wall temperatures at the beginning and end of the upper hot patch do not change with time and are at higher temperatures (875 K), indicating there is no quench-front propagation from the top of the test section.

The measured power in the lower hot patch for Run 176 was reported as 506 W, and the calculated total energy supplied by the lower hot patch to the fluid was 345 W. The 161-W difference between the calculated and measured values indicates a relative error of 32%. These results clearly show that the hot-patch model is capable of arresting the quench front at the beginning of the hot patch while providing a reasonable calculation of the energy to the fluid.

Other runs showed similar characteristics for convergence to steady-state conditions. Therefore, snap-shot results of calculations at a time of 250 s were used for the steady-state data-model comparison unless otherwise mentioned. In addition, the relative error between predicted and calculated parameters is defined as the absolute value of the ratio of the difference between measured and calculated parameters to the measured parameter.

3. Assessment of the Final Model with the Winfrith Steady-State Post-CHF Data. Winfrith Run 176 was selected as a reference run, and assessment results are discussed in detail for this run. Comparisons to indicate the predicted parametric trends are made relative to Run 176.

The predicted void fractions and interfacial drag coefficients for Run 176 as a function of test section height are shown in Fig. 8. Figure 8 also indicates the calculated locations of the quench front, transition boiling, smooth IAF, rough-wavy IAF, and agitated IAF. They are 0.16137 m, 0.16287 m, 0.17551 m, 0.2143 m, and 0.2343 m, respectively. The void fraction in Cell 2 is about 1%. It gradually increases to 96% at the end of test section. As calculated void fractions are less than 98%, the highly dispersed IAF is not predicted to occur in this run. The region downstream of hot-patch experiences the post-agitated IAF (dispersed flow with larger drop diameters) regime. The drag coefficient in Cell 2 is calculated as 381 kg/m^4, with 93.7% of Cell 2

experiencing nucleate boiling and the remaining part in smooth IAF. Cell 3 experiences smooth and rough-wavy IAFs (64% in smooth IAF and 36% in rough-wavy IAF). The drag coefficient in Cell 3 is determined as 218 kg/m^4. Cell 4 experiences rough-wavy IAF. The interfacial drag coefficient is calculated as 215 kg/m^4. In the agitated and post-agitated IAFs, the IFDC decreases, and the void fraction increases gradually toward to the end of the test section.

Direct comparison of the calculated axial void fraction and IFDC profiles with experimental data is not possible because of the lack of experimental pressure drop or void fraction data. However, this comparison can be done indirectly on an integral basis by comparing the calculated and measured (inferred) actual qualities. The measured actual quality at the end of the test section can be evaluated using the following thermodynamic relationship:

$$X_{ac}=X_{equ}\frac{H_{fg}}{H_v(T_v,P_{sat})-H_l(T_{sat},P_{sat})} ,$$

where

X_{ac} = actual quality,
X_{equ} = equilibrium quality,
H_{fg} = heat of evaporation,
$H_v(T_v,P_{sat})$ = enthalpy of vapor at vapor temperature of T_v and saturation pressure of P_{sat}, and
$H_l(T_{sat},P_{sat})$ = enthalpy of liquid at T_{sat} and P_{sat}.

The reported equilibrium quality at the location of 915 mm from the lower hot patch was 10.56%. The vapor temperature was measured 25 mm downstream of this location. Assuming that the vapor temperature at 915 mm is the same as that measured (738 K) at 940 mm, one can calculate an actual quality at this location using the above thermodynamic relation to be 7.99%.

Cell 15 of the TRAC model contains the 915-mm location. The actual quality in Cell 15 also can be calculated from the void-quality relation shown below.

$$\alpha=\frac{1}{\frac{1-X_{ac}}{X_{ac}}\frac{\rho_v}{\rho_l}\frac{V_v}{V_l}+1} ,$$

where

α = void fraction = 0.952,
V_v = vapor velocity = 13.1644 m/s,
V_l = liquid velocity = 2.07646 m/s,
ρ_v = vapor density = 0.64565 Kg/m^3, and
ρ_l = liquid density = 943.12 Kg/m^3.

An actual quality of 7.86% is obtained using the phasic velocities and properties calculated by TRAC and noted above. The calculated actual quality of 7.86% agrees with the inferred measured data of 7.99% and indirectly indicates that the predicted void fractions, and correspondingly the drag coefficients, are reasonable from an integrated standpoint.

The calculated and measured wall and vapor temperatures for Run 176 are shown in Fig. 9 as a function of height. The locations of the flow regimes and hot patches also are indicated in the figure. The quench front (indicated as the CHF point) is located just 2.6 mm upstream of the lower hot patch. The first half of the lower hot patch experiences smooth IAF, whereas the other half is in rough-wavy IAF. The calculated phasic heat fluxes, wall-to-liquid (Denham and near-wall contributions) and wall-to-vapor (Webb-Chen), are presented in Fig. 10. In smooth IAF, the wall-to-liquid heat flux is relatively high and decreases sharply with increasing height. The heat transfer is governed by the wall-to-liquid contribution, and no wall-to-vapor contribution is assumed in this regime. The calculated wall temperatures suggest that the wall-to-liquid heat transfer is predicted reasonably well.

The trend of wall temperature in the second half of the hot patch (where rough-wavy IAF starts) changes. The wall temperature decreases to 830 K at the end of rough-wavy IAF, which is located 0.2143 m from the test section inlet. The calculated and measured wall temperatures imply that the wall-to-liquid heat transfer is predicted well in rough-wavy IAF. The near-wall liquid contribution gradually increases with increasing height. The wall-to-liquid heat transfer contribution by the Denham correlation gradually decreases but is still mainly responsible for transferring the energy from the wall in rough-wavy IAF.

The predicted wall temperature in agitated IAF decreases further and is overpredicted by about 10°C at the end of the agitated region. In this region, no void fraction weighting is applied to the near-wall wall-to-liquid HTC. Therefore, the wall-to-liquid heat flux does not vary significantly, as shown in Fig. 10. It decreases very slowly until the axial location, where the void fraction becomes about 45%. After this location, it gradually decreases because of the applied void-dependent

weighting. The wall-to-vapor heat flux increases with increasing height but still increases relatively less in comparison to the wall-to-liquid heat flux.

The interfacial heat-transfer model uses a relatively high HTC for the heat transfer from the interface to the vapor in smooth, rough-wavy, and agitated IAFs. Therefore, the calculated vapor temperatures are close to the saturation temperature of the fluid. In post-agitated IAF, the interface-to-vapor HTC drops to very low values. It has been observed experimentally that the evaporation process in dispersed flow is inefficient relative to that just downstream of the CHF point (8). The axial vapor temperature profile measured was S-shaped, low or close to the saturation temperature in the region near to the CHF point, and high in the dispersed flow region (far-region of the CHF point) (9). Using a weighted interface-to-vapor HTC allows the vapor temperature to be superheated gradually in post-agitated IAF, as shown in Fig. 9.

The wall temperature at the beginning of the post-agitated IAF increases with increasing axial distance. The calculated wall temperatures between 0.23–0.45 m are about 10°C higher than measured values. After 0.5 m, the agreement between calculated and measured wall temperatures becomes very good. The slope of the wall temperature profile agrees with experimental data, indicating that the overall wall-to-fluid heat transfer is predicted very well in this region. The near-wall wall-to-liquid heat flux decreases with increasing height, as shown in Fig. 10. At 50 cm, it is about 40% of the wall-to-vapor heat flux, whereas it becomes approximately 6% of the wall-to-vapor heat flux at the end of the test section. The predicted vapor temperature increases gradually and becomes 649 K in the 16th cell, whereas the measured vapor temperature was 738 K, indicating an 89°C under-prediction (a 12% relative error). It can be concluded that the overall predictions of the interfacial and wall-to-fluid heat transfer for Run 176 agree with the experimental data reasonably well.

Figure 9 also shows the calculated and measured axial wall and vapor temperature profiles for Run 179. Run 179 has a 45% lower heat flux than Run 176 while retaining the same mass flux and pressure. The locations of the IAFs are similar to those observed in Run 176. This is because Ishii's flow regime criteria consider the capillary number defined at the CHF point, which is similar in Runs 176 and 179. The predicted heat transfer in smooth and rough-wavy IAFs showed good agreement with the measured data. However, it slightly over-predicted the agitated and post-agitated IAFs. Therefore, the wall temperatures are under-predicted by about 60°C at 0.3 m. However, the predicted and measured wall

temperature profiles in post-agitated IAF agreed with each other very well. The predicted vapor temperature is approximately 100°C lower then the measured value. This also causes the wall temperature to be shifted slightly to lower values. The under-prediction of the wall temperature indicates a relative error of 8%. The trend of the wall-to-fluid and interfacial heat transfer with the heat flux is predicted reasonably well; a decrease in wall heat flux decreases wall and vapor temperatures.

In Fig. 11, we plot the predicted and measured wall and vapor temperatures for Runs 136 and 194. These two tests were conducted with nearly constant pressure, heat fluxes, and inlet temperatures but with different mass fluxes—a mass flux of 49 kg/m^{2}s for Run 136 and 199 kg/m^{2}s for Run 199. The wall temperatures for Run 136 agreed with the experimental data within the smooth and rough-wavy IAFs, whereas they were under-predicted by about 60°C (indicating a relative error of 4%) in the agitated and post-agitated IAFs. However, the rate of increase in wall temperatures in the post-agitated IAF agreed with the experimental data. The vapor temperature increases at the same rate as the wall temperature, indicating a very inefficient interfacial heat transfer. The vapor temperature at the end of the test section is under-predicted by about 100°C (which corresponds to an 11% relative error). The increase in inlet mass flux for Run 194 decreases measured wall and vapor temperatures and also is observed in the predictions. The wall temperatures at the higher mass fluxes are in very good agreement with the experimental data until 0.6 m, where a slight under-prediction begins. At the end of the test section, the wall temperatures were under-predicted by about 40°C. However, this under-prediction is only a 5% relative error. Thus, the trend of predicted wall temperatures with the mass flux is predicted correctly.

The effect of pressure is investigated in Fig. 12 by plotting the predicted and measured wall and vapor temperatures for Runs 150 and 135. The pressure of Run 150, 2 bar, is increased to 10 bar in Run 135. These runs were performed with same mass fluxes (lowest mass flux of Winfrith post-CHF data base) and approximately the same heat fluxes and inlet subcoolings. The predicted wall and vapor temperatures at the lower pressure (Run 150) are in reasonably good agreement with the experimental data. The measured wall and vapor temperatures decrease with increasing system pressure. This trend also is seen in predicted wall and vapor temperatures except that predicted wall and vapor temperatures are about 100°C and 200°C less than measured values, respectively. The heat flux in Run 135 is 35% higher than that of Run 150. Therefore, there is an offsetting effect to that exhibited by the pressure. Again, the measured and predicted wall temperature profiles do

show good comparison when the 100°C offset at 0.3 m is noted. In Run 135, relative errors of 13% and 20% are evident for predicted wall and vapor temperatures, respectively.

Figure 13 shows the results obtained for two extreme cases; a high heat flux and pressure (Run 76) and a very high mass flux (Run 95). The predicted wall temperatures in smooth, rough-wavy, and agitated IAFs in Run 76 agree with the experimental data. As the axial distance increases, the prediction of wall temperature deviates from measured data and indicates a 100°C under-prediction of the wall and vapor temperatures at the end of test section. The relative errors are 9% and 12%, respectively. For Run 95, it is clear that the wall-to-fluid heat transfer is under-predicted in all IAFs. The slopes of predicted and measured wall temperatures in post-agitated IAF are in reasonably good agreement. Almost no vapor superheat is predicted for Run 95, as expected. It can be concluded that even for these extreme cases, the prediction of the wall-to-fluid and interfacial heat transfers are reasonable.

Figure 14 summarizes the results obtained for different subcoolings. The inlet subcooling in Run 193 is increased by 20°C more than that of Run 161. The wall heat fluxes were reasonably constant, with a 13% difference. Runs 161 and 193 had the same mass fluxes and pressures. The results obtained for Run 161 indicate that wall and vapor temperatures are under-predicted, especially just downstream of the CHF point. The prediction becomes reasonable in this region when the subcooling is increased in Run 193. In Run 193, the wall temperatures at the end of the test section agreed with experimental data; they were over-predicted at the beginning of the post-agitated IAF. The measured wall and vapor temperatures decrease with increasing inlet subcooling. The predicted wall temperature profiles did not show this trend; in fact, wall temperatures were over-predicted about 10°C in Run 193. We can conclude at least that the model predicts the experimental trend in smooth, rough-wavy, agitated IAFs with increasing inlet subcooling but needs further work in the post-agitated regime.

C. The Predicted Quench Histories

The clad temperatures and the rate of the quench-front propagation, which are the two most important parameters in nuclear reactor safety analyses, are predicted as a result of the code-calculated solution for the coupled differential equations of the fluid mechanics and the heat conduction. The prediction of the clad cooling rate throughout the core strongly depends on the prediction of the correct

void fraction distribution. As discussed previously, the pressure drops predicted by the interfacial drag model were reasonable, indicating reasonable prediction of the void fraction histories along the heater rods. Also, the wall temperatures and their steady-state spatial variation in the film boiling region have been shown to be reasonable. The predicted wall temperature histories and the quench-front velocities for a Lehigh reflood run and CCTF Run 14 are discussed below.

The predicted and measured wall temperatures at the 0.15-, 0.3-, and 0.45-m elevations above the test section inlet are plotted against the transient time for the Lehigh reflood test in Fig. 15. Generally, the agreement between predicted and measured values is reasonable. In the first 10 s of the transient, the predicted wall temperatures agree with measured values, indicating that the boundary and initial conditions are specified correctly. The 15-cm elevation is located at the end of the first cell. In the first 10–20 s in transient calculations, the drag coefficient in the first cell is over-predicted. This causes the vapor velocity, and correspondingly the length of the transition boiling, to be calculated as relatively high. Thus, the quench front propagates with relatively higher rates, resulting in an early prediction of the quench time by about 25 s.

The overall rate of decrease in wall temperature (between 0–100 s) at 30 cm is in reasonably good when compared with the experimental data. There are some oscillations in the predicted wall temperatures. These are associated with void fraction oscillations that exist in the calculation (3). The predicted quench time agrees with the experimental data, but the rate of decrease in the predicted wall temperature at 45 cm is slightly over-predicted. This causes an under-prediction of the wall temperatures before this location is quenched. The predicted quench time at this elevation agrees with the measured data. Figure 16 shows the predicted and measured wall and vapor temperature histories at an elevation 60 cm downstream of the inlet. The wall temperatures and its slope are predicted reasonably well. However, the predicted vapor temperatures are 200°C lower than measured values.

The predicted and measured rewetting velocities between 0.15, 0.30 and 0.45 m are listed in Table 1. Table 1 indicates that the quench velocity at the lower elevations show some disagreements. However, it becomes stable and agrees with the experimental data at higher elevations (or later in the transient).

The above comparison indicates that the model predicts the quench histories (the quench time and the quench-front velocities) reasonably well for the Lehigh run under consideration. This conclusion is also true for CCTF Run 14, as indicated

in Fig. 17, which shows the predicted and measured wall temperature histories at the 0.38-, 1.015-, and 1.83-m elevations.

In Fig. 17, the rate of decrease in wall temperature in the lower part of the core (0.38 and 1.015 m) agreed with measured data, indicating that the overall heat transfer is predicted well. The quench time at 1.015 m is predicted about 23 s later than the experimental data. The vapor Reynolds number at the quench front during this time varies around 2000 when the quench front progresses to this elevation, causing the B-coefficient used in the transition boiling to change frequently between 10 and 16. This slows the quench-front propagation rate. At 1.83 m, the precursory cooling rate is slightly over-predicted until 250 s, resulting in an under-prediction of the wall temperatures. The increase in measured wall temperatures levels off at about 150 s. whereas the predicted wall temperature levels off 50 s later. This is because the void fraction at this elevation does not begin a significant decrease early enough (see Fig. 2). There is also an interaction with the heat transfer and the unheated-wet-wall model during this time. The unheated-wet-wall effect is most significant at the higher void fractions, and thus, too much cooling results for liquid that may be distributed in a film and generally not available for cooling. After 200 s, the predicted wall temperature decreases at the same rate observed in the experimental data.

The quench times are in good agreement with the experimental data. The predicted and measured quench times at three axial elevations and the averaged rewetting velocities between these axial elevations are listed in Table 2. Table 2 indicates that the thermal-hydraulic model for post-CHF convective heat transfer used in TRAC computer program also is able to predict the rewetting velocity reasonably well for CCTF Run 14 reflood test.

III. SUMMARY AND CONCLUSIONS

The following conclusions can be drawn from the results discussed above.

1. The nucleate boiling interfacial drag model predicted the CCTF Run 14 pressure drop data well in the low- and high-void-fraction region. The pressure drop in the intermediate void fraction nucleate boiling region was slightly over-predicted.

2. The pressure drop in IAFs were slightly under-predicted at lower void fractions and over-predicted at higher void fractions. The predicted pressure drop was in reasonable agreement with the measured data in the intermediate void fraction region, where the IFDCs were obtained by weighting functions between the low- and high-void-fraction regions.

3. The pressure drop was under-predicted in the upper part of the core in the CCTF Run 14 test. The under-prediction was attributed to the IFDC model of the wet unheated walls. The IFDC model for the highly dispersed flow gave reasonable results for the Lehigh pressure drop data that did not include any unheated wall effects.

4. The hot-patch model was capable of modeling Winfrith steady-state post-CHF experiments. It predicted reasonable energy input to coolant from the bottom hot patch and did not allow any quench front propagation from either the bottom or top.

5. The transient calculations converged to steady-state conditions in relatively short times for the conditions of the Winfrith tests studied in this work. The calculated thermal-hydraulic parameters at 250 s were used for steady-state post-CHF data-model comparisons.

6. Comparison of calculated and measure (inferred) actual qualities at the end of the test section showed good agreement. This indirectly verified that the core reflood interfacial drag model predicted the void fraction and interfacial drag coefficients reasonably.

7. In general, the interfacial heat-transfer model under-predicts the vapor temperature. However, the model predicted its variation with the operating parameters reasonably well for operating conditions studied in this paper and is expected to predict for a larger range of operating parameters. The maximum difference between calculated and measured vapor temperatures was 20% and found at the test pressure of 10 Bar (Run 135)

8. The wall-to-fluid heat transfer was predicted reasonably well for the operating parameters of the Winfrith data discussed in this paper and is expected to predict a larger range of operating parameters. The maximum relative error between the predicted and measured wall temperatures was less than 13%. Additional work is needed in this area to better understand the effects of subcooling and heat fluxes.

9. The thermal-hydraulic model for post-CHF convective heat transfer used in TRAC computer program was able to predict the rewetting velocity reasonably well for the Lehigh and CCTF Run 14 reflood tests. The average slope of the wall temperature trace showed reasonably good agreement with the measured data.

10. Although they are not formulated as mechanistic models, the formulation of the near-wall liquid effect and the transition boiling models gave reasonable results in predicting wall-to-fluid heat transfer and the quench-front propagation. There is a need for further work for the axial-dependent transition boiling model and the near-wall liquid effects. The results discussed in this paper indicate that the capillary and vapor Reynolds numbers defined at the CHF point could be the proper dimensionless numbers for the modeling transition boiling. The vapor Reynolds number also determines the near-wall liquid contribution. The functional form of this contribution indicates that it should increase gradually up to the agitated IAF, become maximum in the agitated IAF, and finally diminish with axial distance in the post-agitated regime.

The results discussed in this paper are presented in the hope of aiding future developments of improved mechanistic models for prediction of post-CHF conditions dealing with the quenching of heated structures. In particular, work is needed in the area of the history-dependent transition boiling model, the near-wall liquid effect, the unheated-wet wall effect, and the IAF interfacial drag models.

REFERENCES

1. R. A. Nelson and C. Unal, "A Phenomenological Model of Thermal-Hydraulics of Convective Boiling During the Quenching of Hot Rod Bundles; Part I: Thermal-Hydraulic Model," submitted for the possible presentation in National Heat Transfer Conference in 1991.

2. C. Unal, K. Tuzla, C. A. Tuzla, and J. C. Chen, "Vapor Generation Model for Dispersed Drop Flow," 1989 National Heat Transfer Conference, ANS Proceedings HTC-Vol. 4, August 6-9, 1989.

3. K. Hirano et al., " Data Report on Large Scale Reflood Test-14, CCTF Test CI-5 (Run 014)," JAERI memo 57-214 (August 1982).

4. D. Swinnerton, M. L. Hood, and K. G. Pearson, " Steady-State Post-Dryout at Low Quality and Medium Pressure Data Report," Winfrith United Kingdom Atomic Energy Authority report AEEW-R 2267 (June 1988).

5. K. Tuzla, C. Unal, O. Badr, S. Neti, and J. C. Chen, "Thermodynamic Nonequilibrium in Post-Critical-Heat-Flux Boiling in a Rod Bundle," NUREG/CR-5095, Volumes 1-4 (July 1987).

6. R. A. Nelson and C. Unal, "A Phenomenological Model of Thermal-Hydraulics of Convective Boiling During the Quenching of Hot Rod Bundles," Los Alamos National Laboratory report in preparation.

7. C. Unal, K. Tuzla, and J. Chen, "A TRAC-PF1/MOD1 Analysis of a Lehigh Rod Bundle Post-CHF Reflood Test," Lehigh University Institute of Thermo-Fluid Engineering and Science report TS-861 (July 1986).

8. C. Unal, K. Tuzla, O. Badr, S. Neti, and J. C. Chen, "Convective Boiling in a Rod Bundle: Transverse of Vapor Superheat Temperature Under Stabilized Post-CHF Conditions," accepted by Journal of Int. Heat Mass Transfer (1990).

9. C. Unal, K. Tuzla, O. Badr, S. Neti, and J. C. Chen, "Convective Film Boiling in a Rod Bundle: Axial Variation of Evaporation Ratio," International Journal of Heat and Mass Transfer **31**, 2091 (October 1988).

TABLE 1
THE CALCULATED AND MEASURED QUENCH TIMES AND QUENCH FRONT VELOCITIES FOR LEHIGH REFLOOD TEST

Location (m)	Quench Time (s)		Quench-Front Velocity[a] (mm/s)	
	Exp.	Calc.	Exp.	Calc.
0.15	62	29.6	2.42	5.1
0.30	111	108	3.1	1.91
0.45	177	178	2.27	2.14
0.60		242		2.31

[a]The quench-front velocity is calculated between locations listed in the table and indicates average values over a 0.15-m distance.

TABLE 2

THE CALCULATED AND MEASURED QUENCH TIMES AND QUENCH FRONT VELOCITIES FOR CCTF RUN 14 TEST

	Location (m)	Quench Time (s)		Quench Front Velocity (mm/s)	
		Exp.	Calc.	Exp.	Calc.
x	0.38	70	72	5.4	5.3
	1.105	151	174	8.9	7.1
	1.83	333	337	4.0	4.4

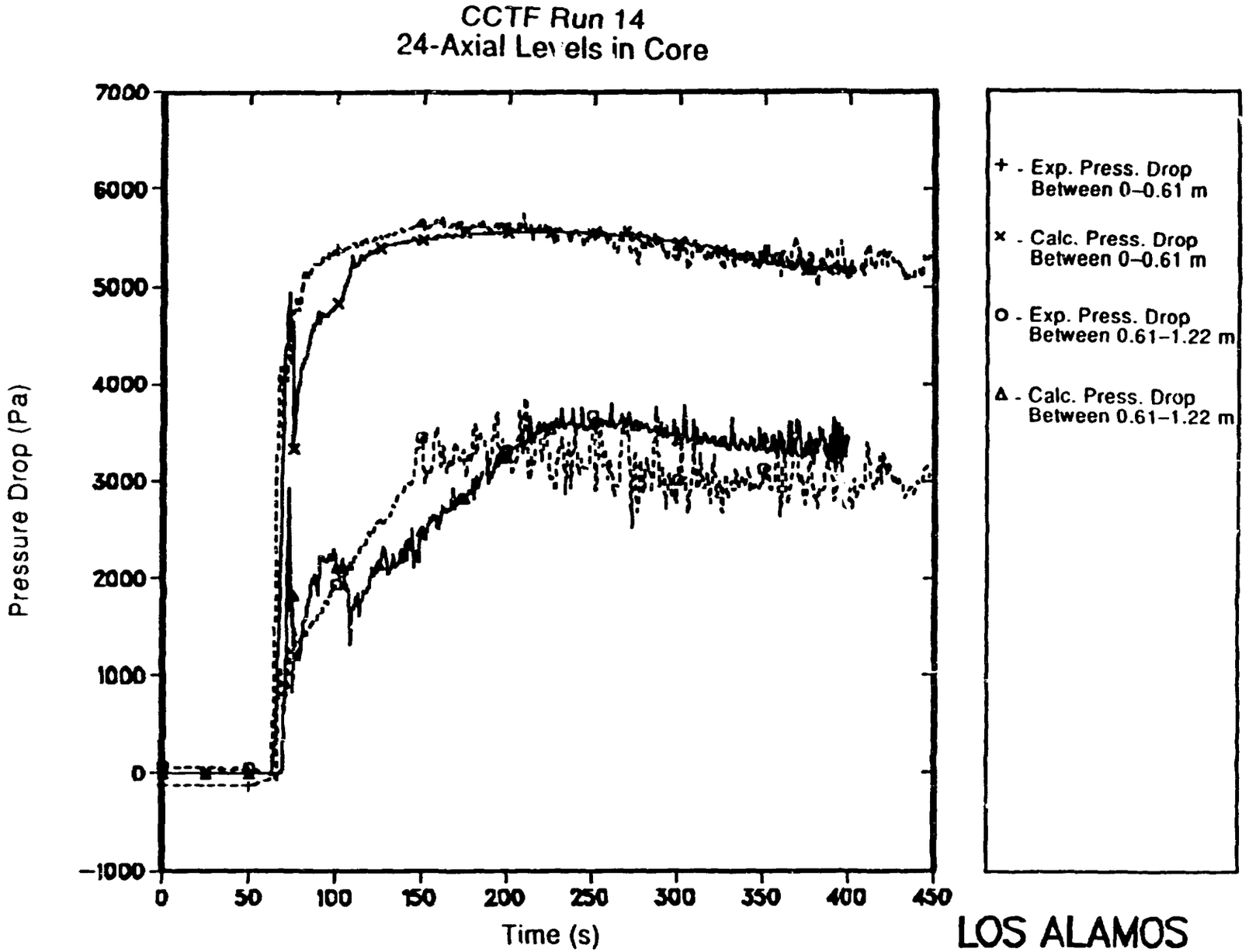

Fig. 1.
The predicted and measured pressure drops between axial locations of 0.0–0.61 m and 0.61–1.22 m for the CCTF Run 14 test.

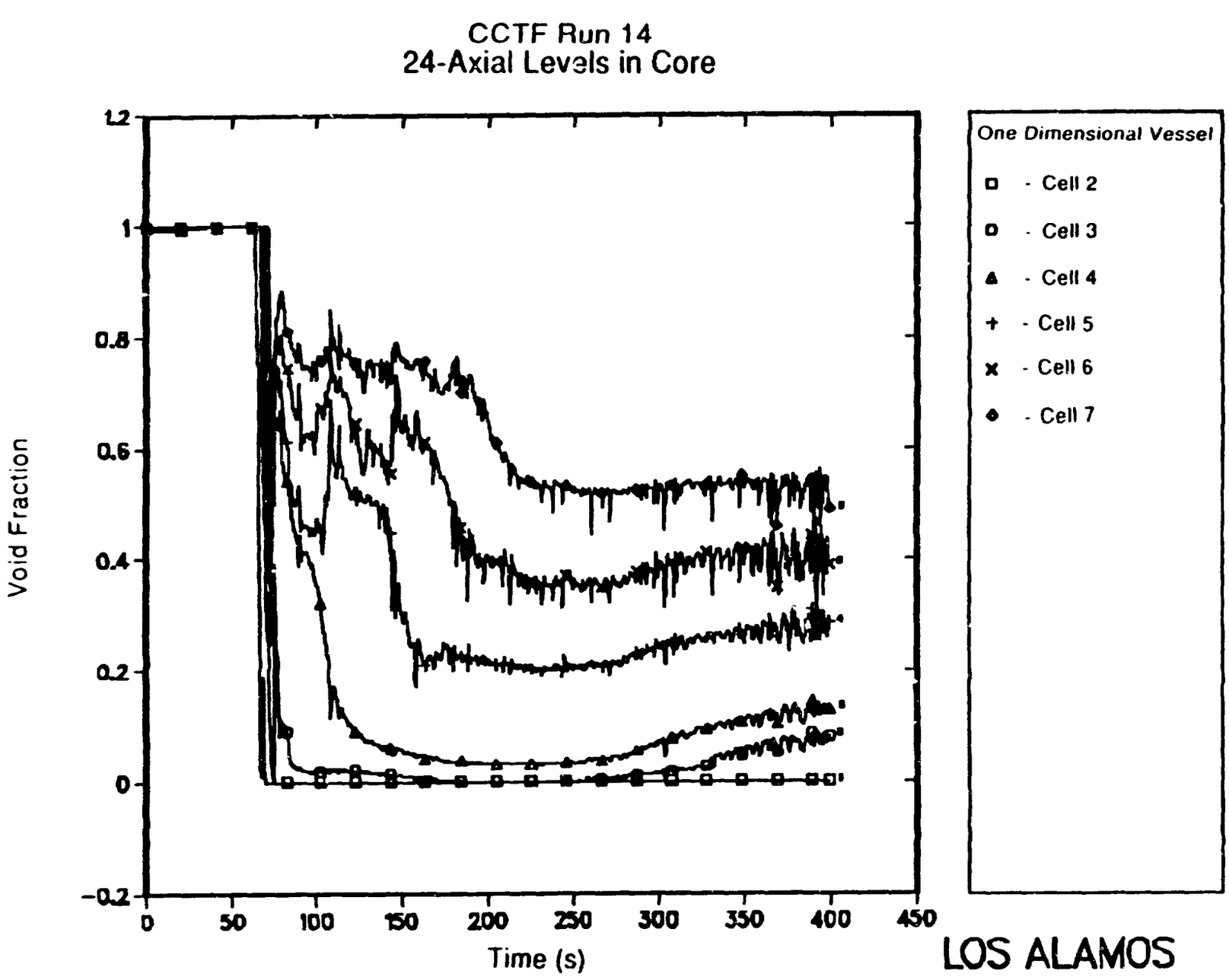

Fig. 2.
The predicted void fractions in Cells 2 to 7 in the CCTF Run 14 test.

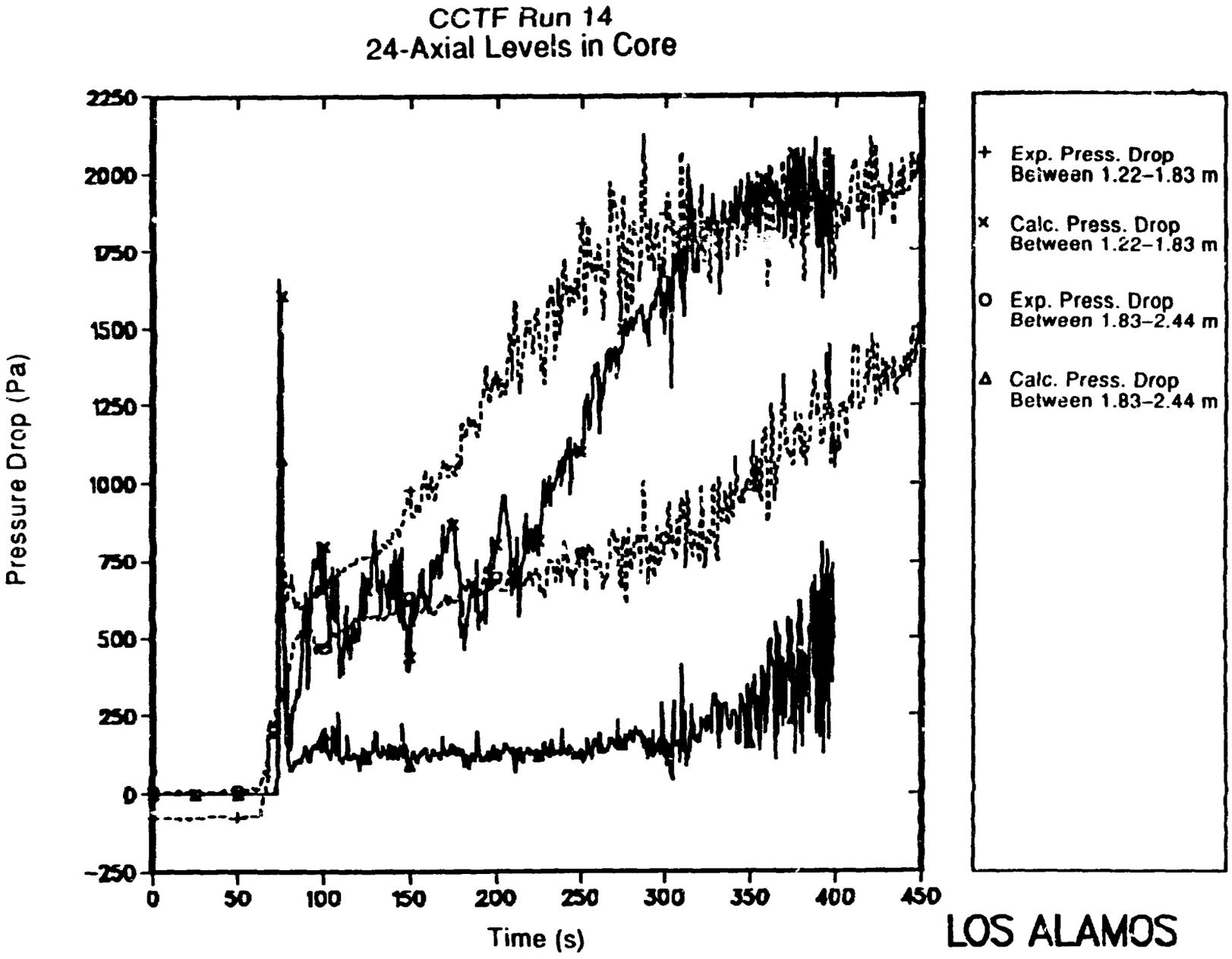

Fig. 3.
The predicted and measured pressure drops between axial locations of 1.22–1.83 m and 1.83–2.44 m for the CCTF Run 14 test.

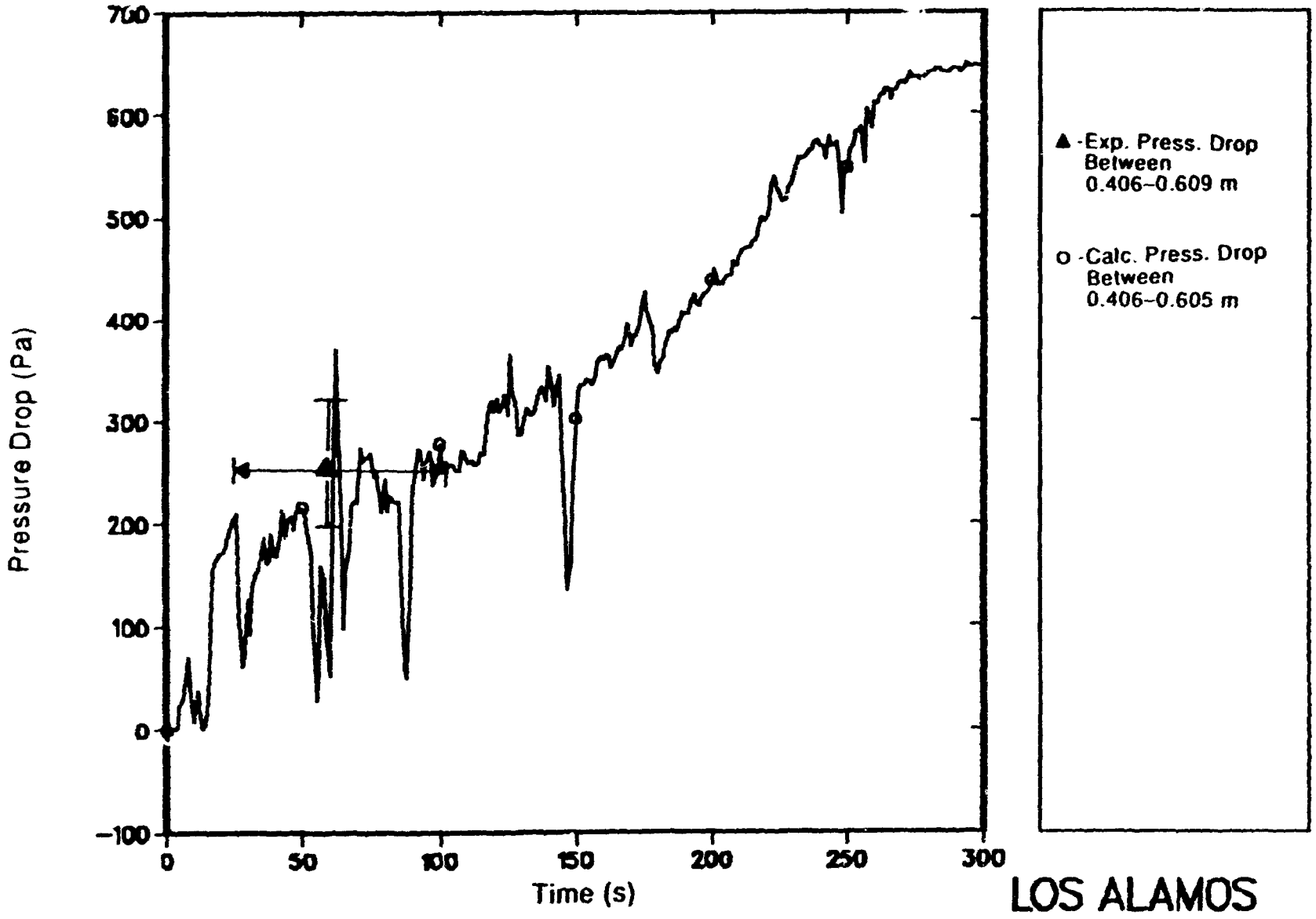

Fig. 4.
The predicted and measured pressure drops between axial locations of 0.406–0.609 m for the Lehigh rod bundle test.

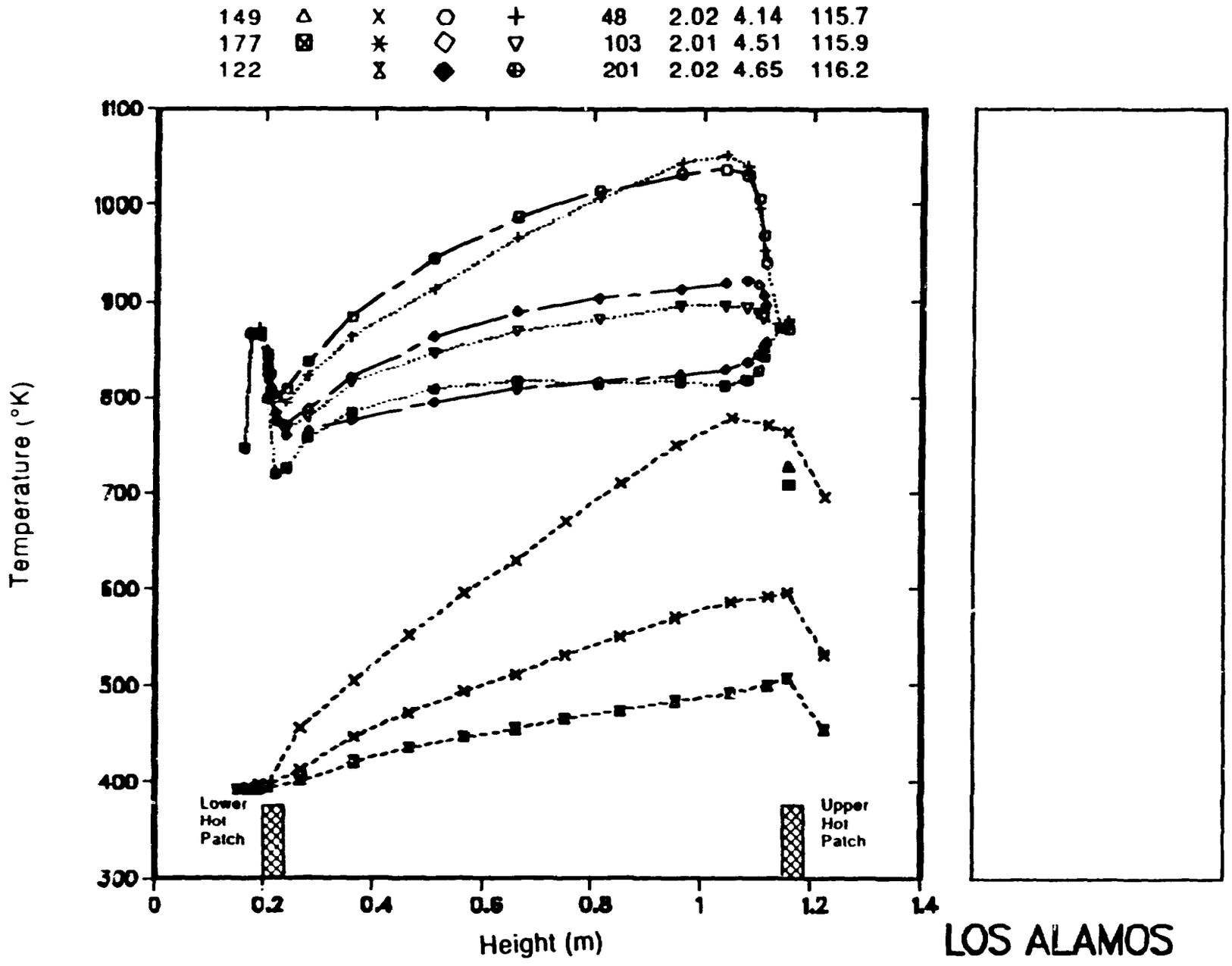

Fig. 5.
The predicted and measured wall and vapor temperature profiles for Winfrith Runs 149, 177, and 122.

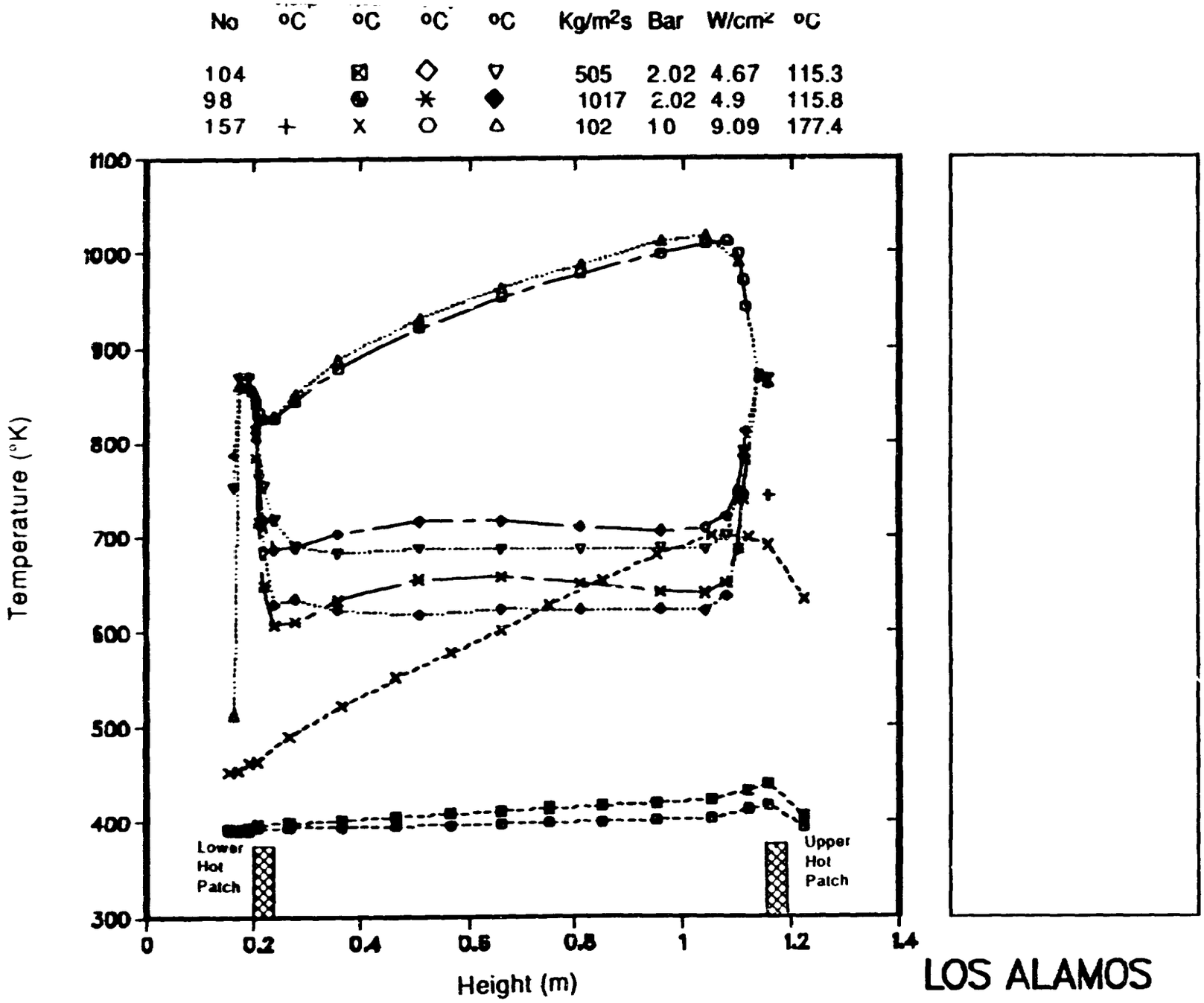

Fig. 6.
The predicted and measured wall and vapor temperature profiles for Winfrith Runs 104, 98, and 157.

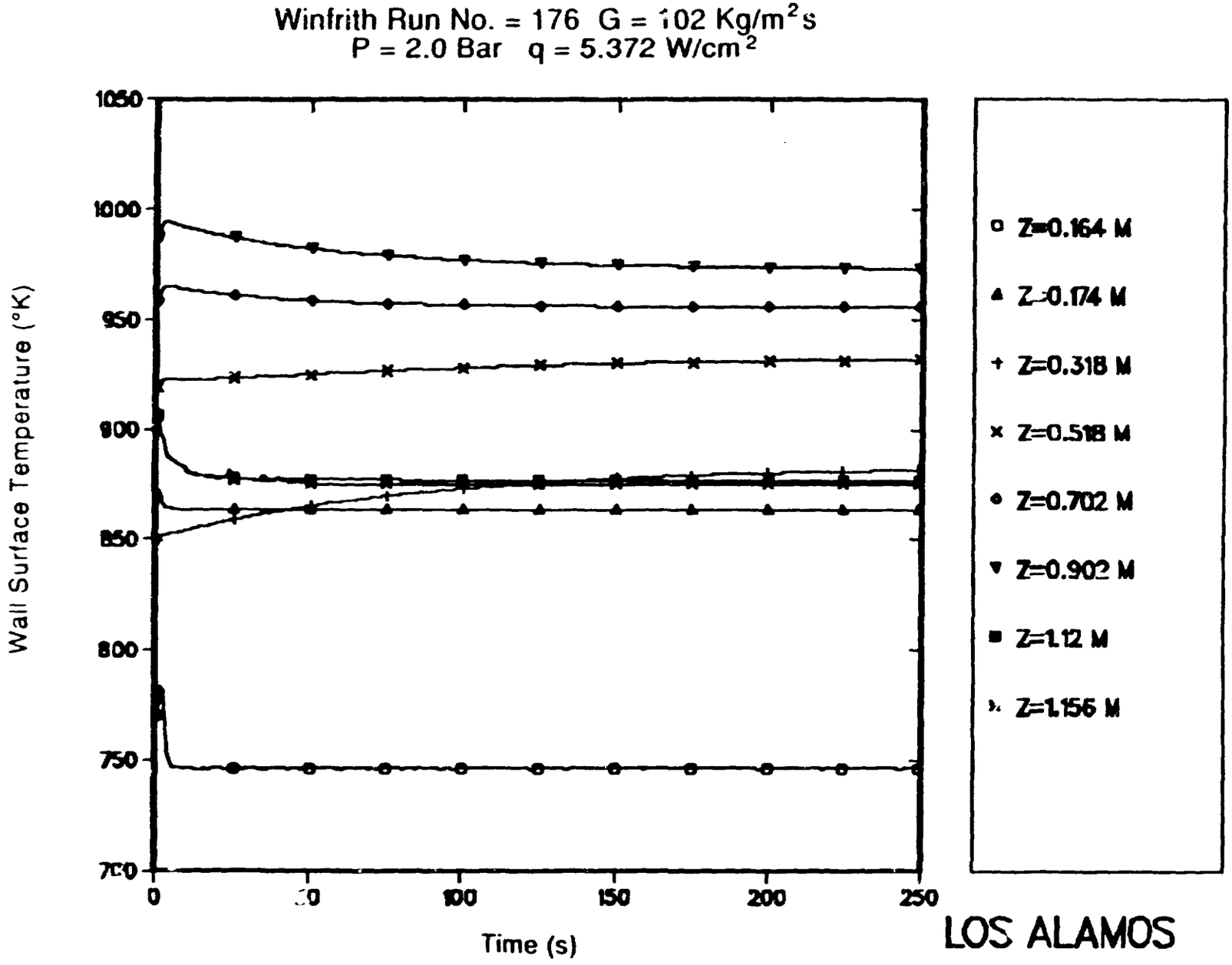

Fig. 7.
The calculated wall surface temperature histories at eight different axial elevations for Winfrith Run 176.

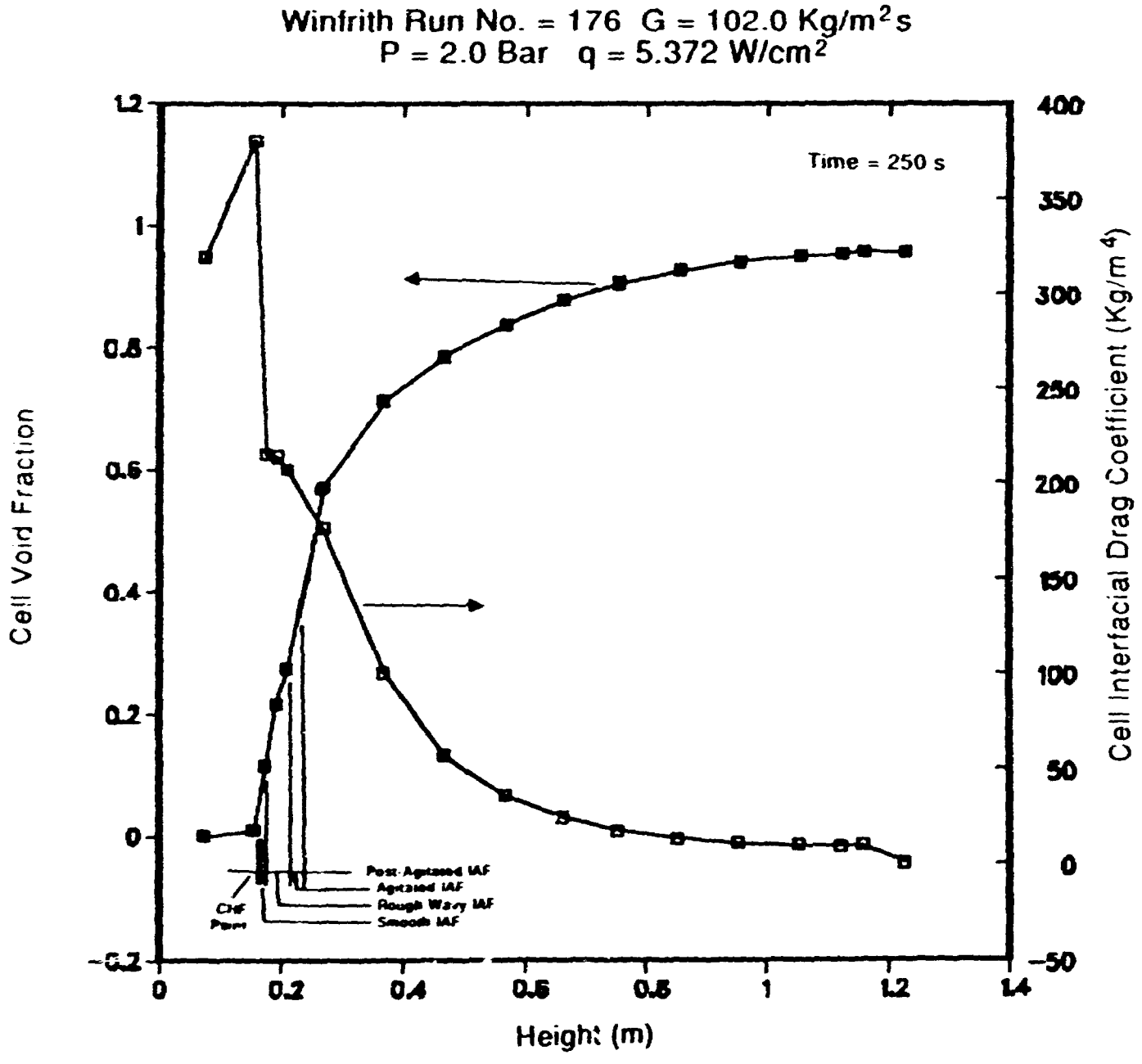

Fig. 8.
The predicted void fractions and interfacial drag coefficients for Winfrith Run 176 as a function of test section height.

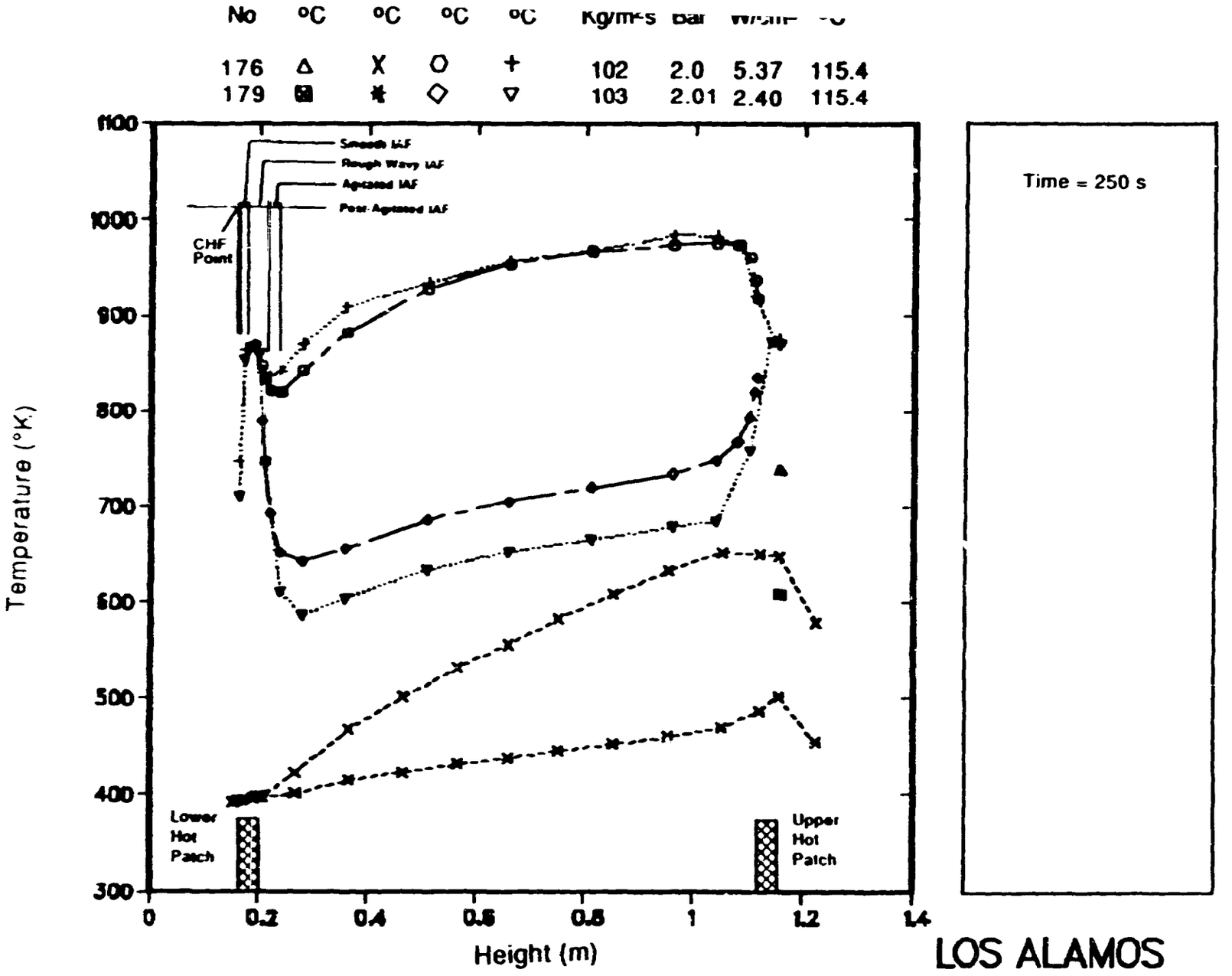

Fig. 9.
The calculated and measured wall and vapor temperatures for Winfrith Runs 176 and 179.

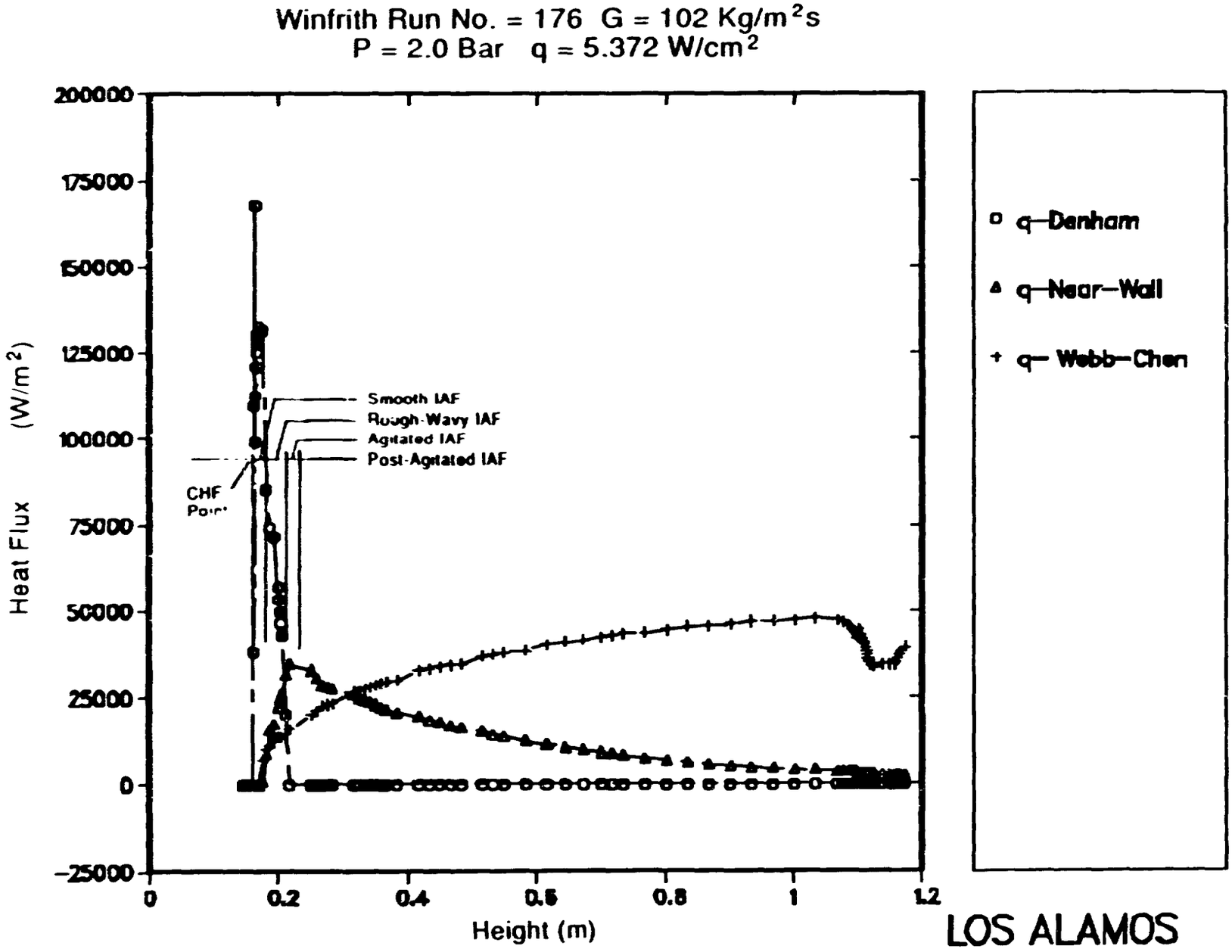

Fig. 10.
The predicted wall-to-liquid and wall-to-vapor heat fluxes as a function of test section height for Winfrith Run 176.

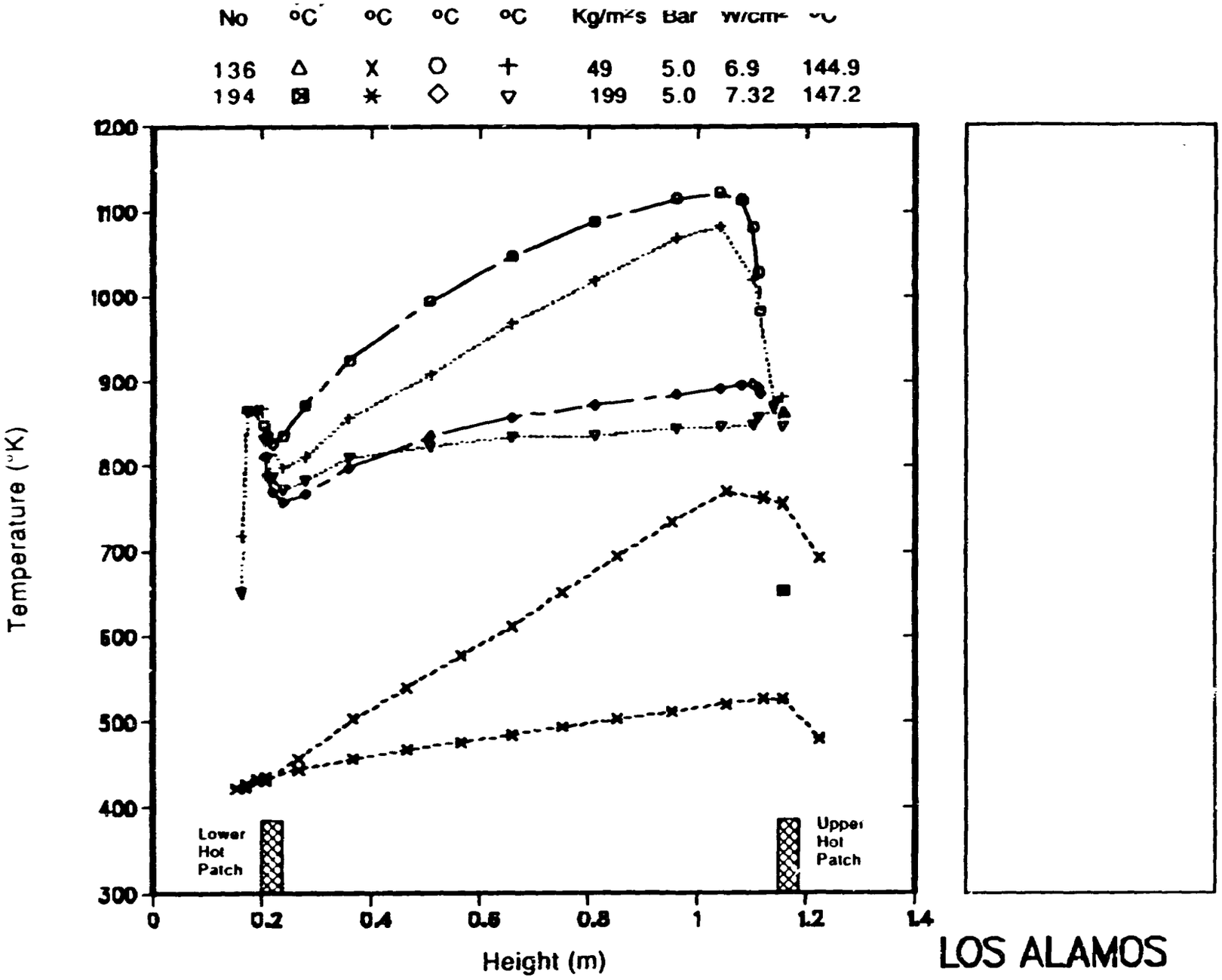

Fig. 11.
The effect of total mass flux on the predicted and measured wall and vapor temperature profiles for Winfrith Runs 136 and 194.

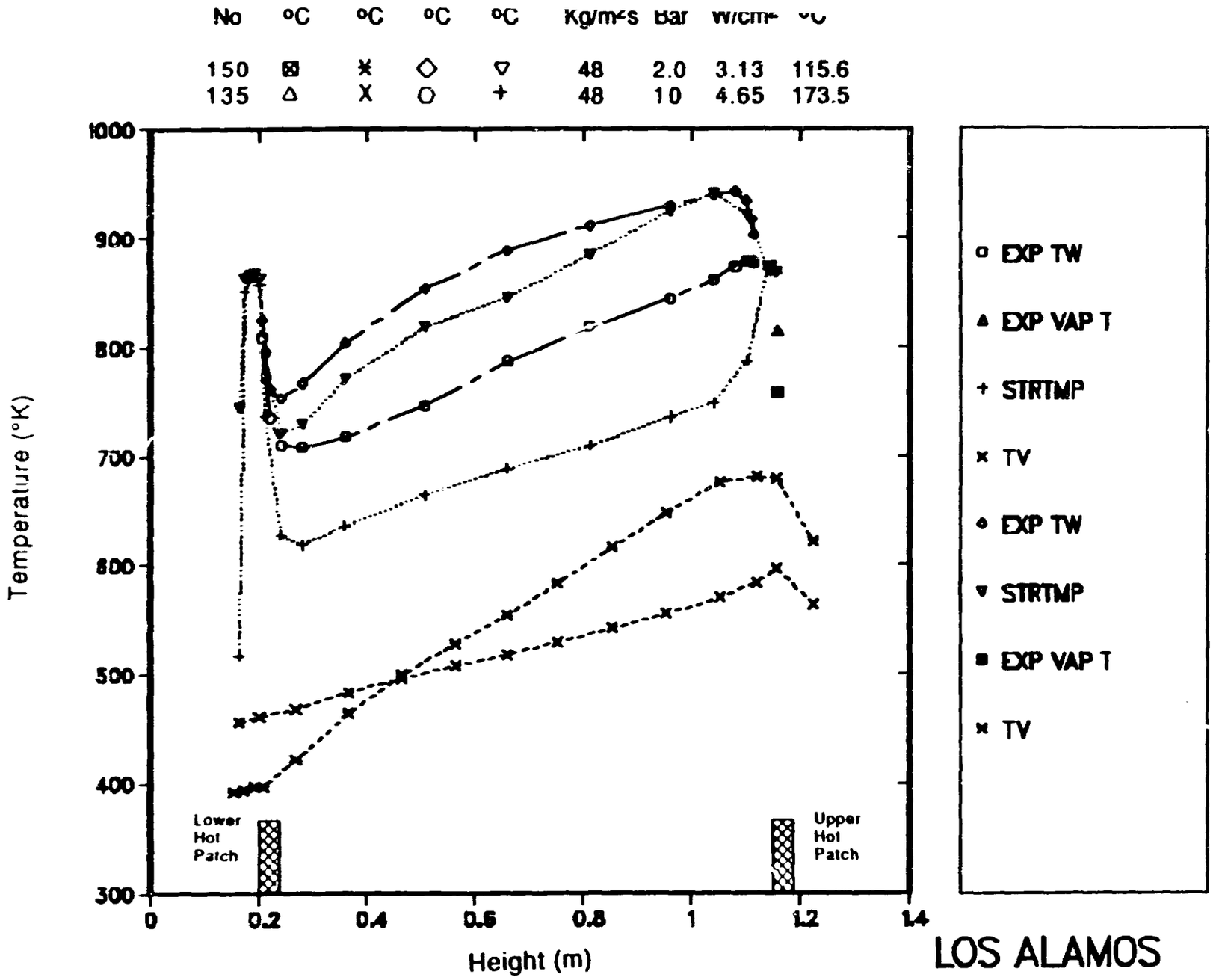

Fig. 12.
The effect of pressure on the predicted and measured wall and vapor temperature profiles for Winfrith Runs 150 and 135.

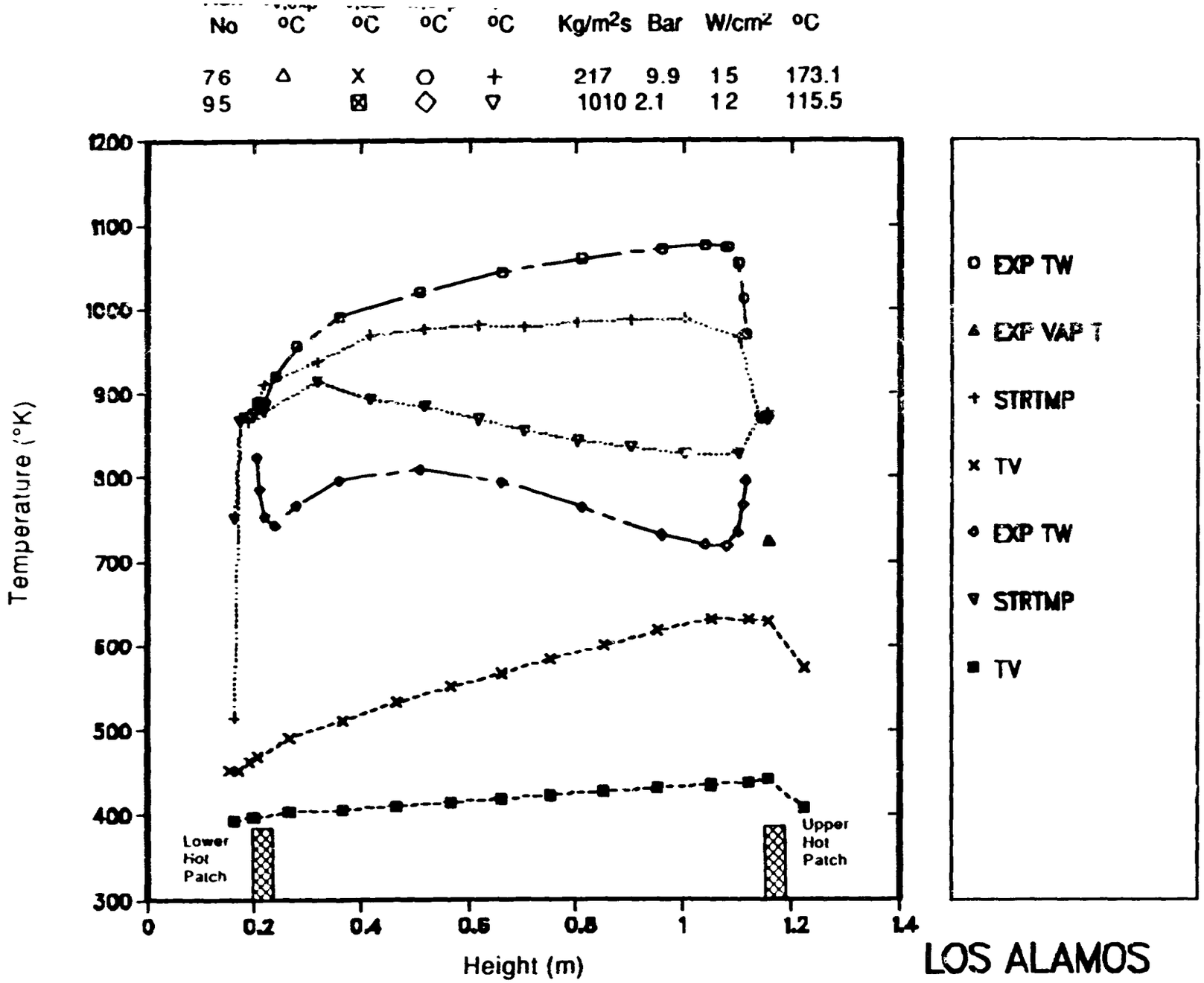

Fig. 13.
The predicted and measured wall and vapor temperature profiles for Winfrith Runs 76 and 95.

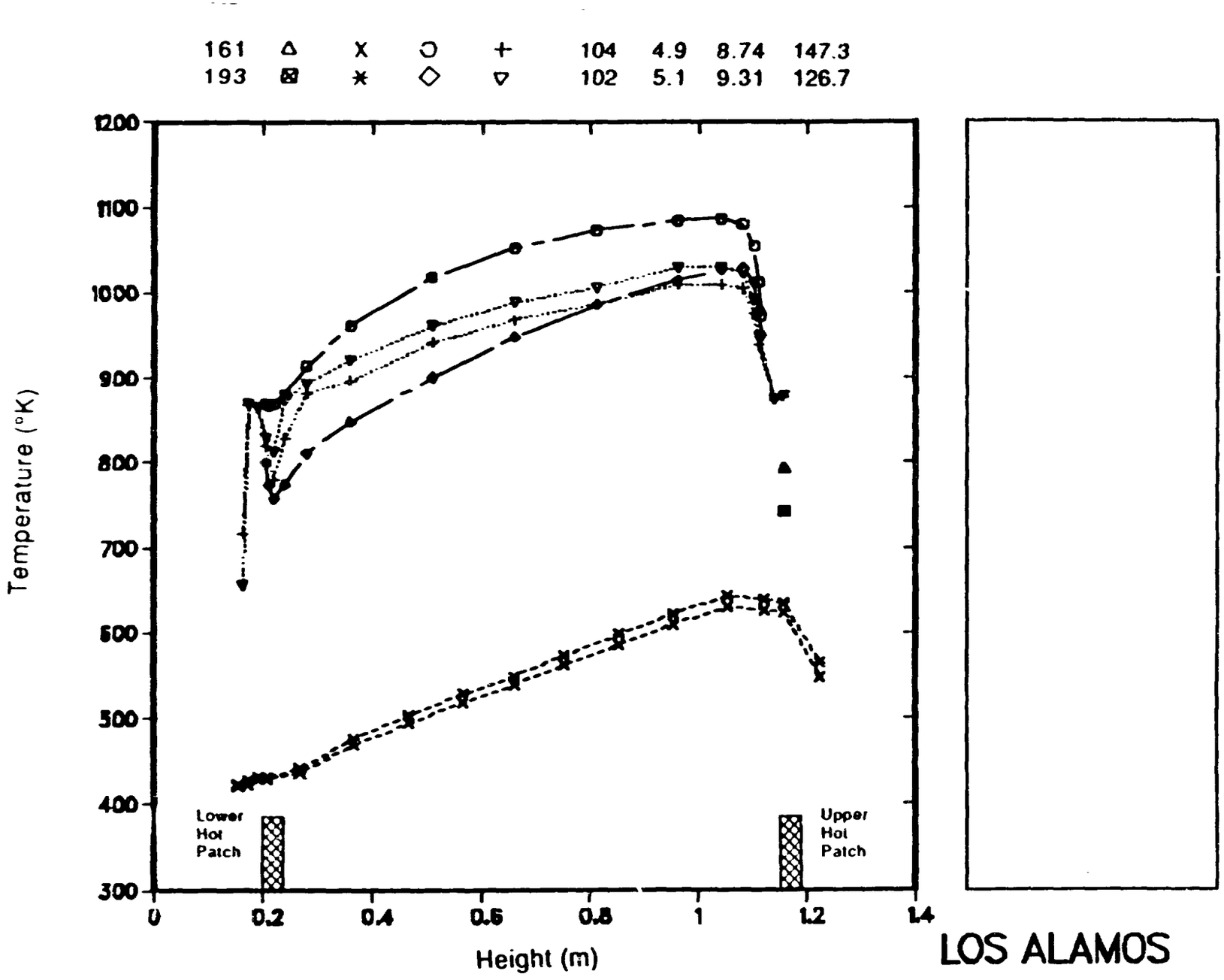

Fig. 14.
The effect of inlet subcooling on the predicted and measured wall and vapor temperature profiles for Winfrith Runs 161 and 193.

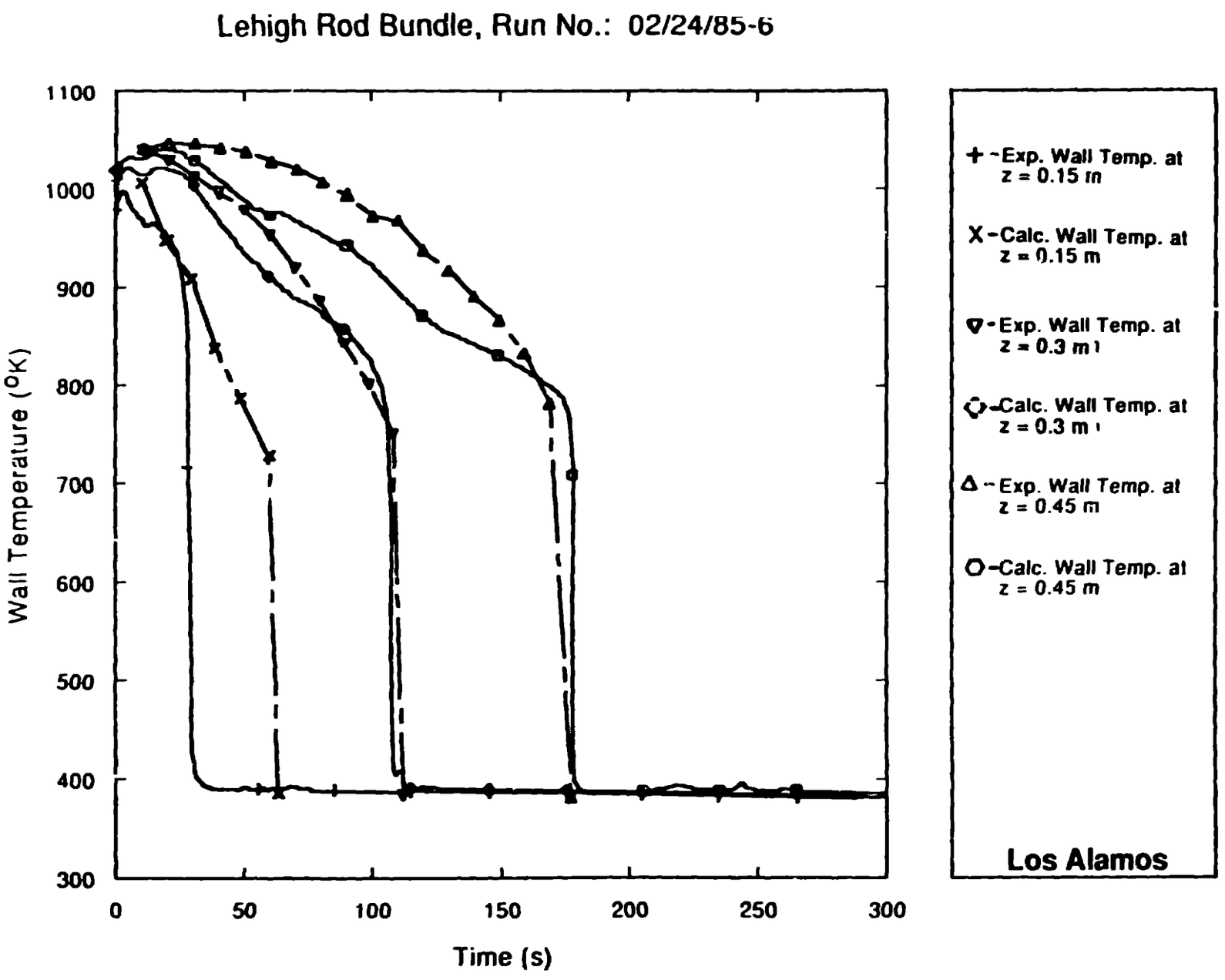

Fig. 15.
The predicted and measured wall temperatures at the 0.15 m, 0.3 m, and 0.45 m elevations above the test section inlet for the Lehigh rod bundle test.

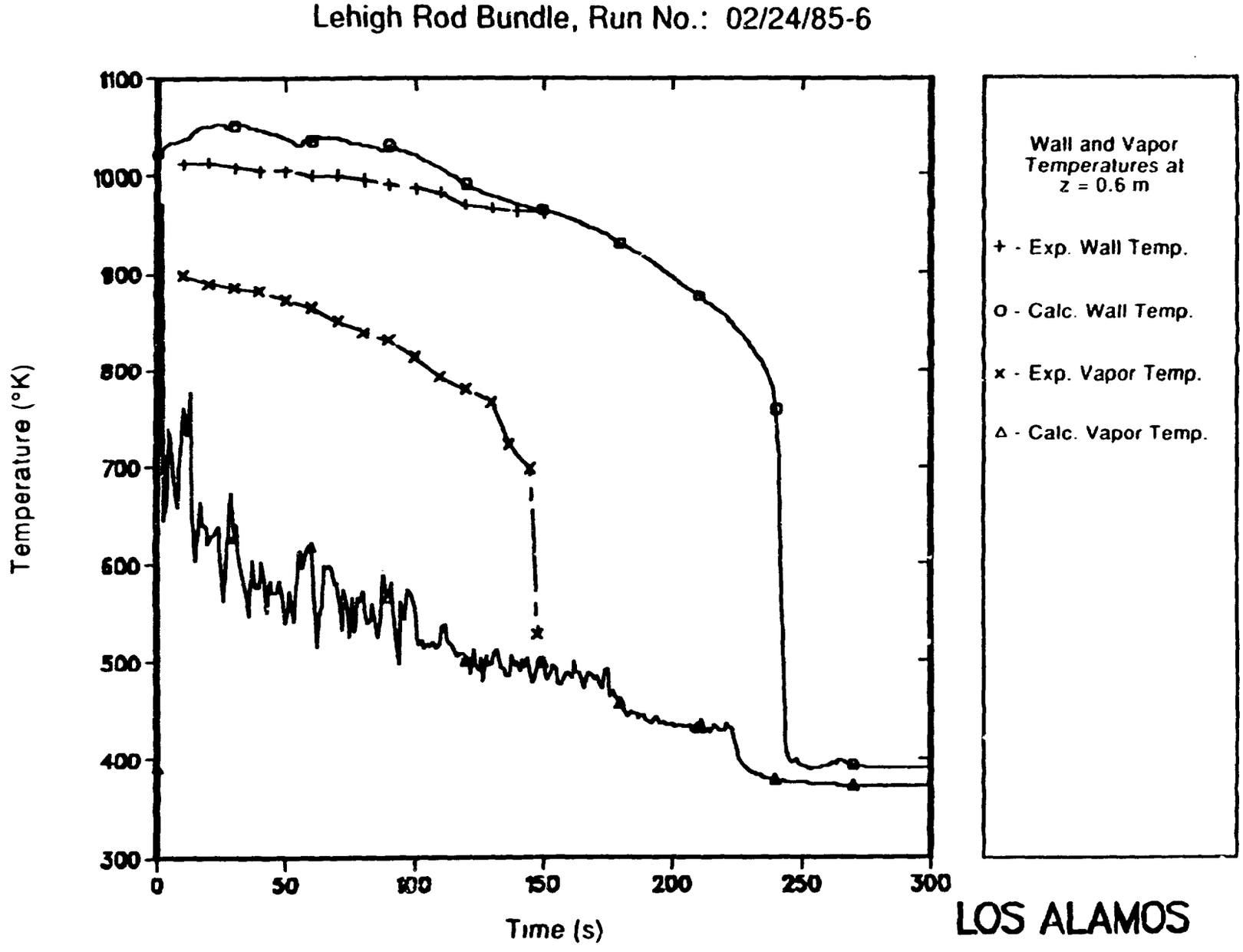

Fig. 16.
The predicted and measured wall and vapor temperature histories at an elevation 60 cm downstream of the inlet for the Lehigh rod bundle test

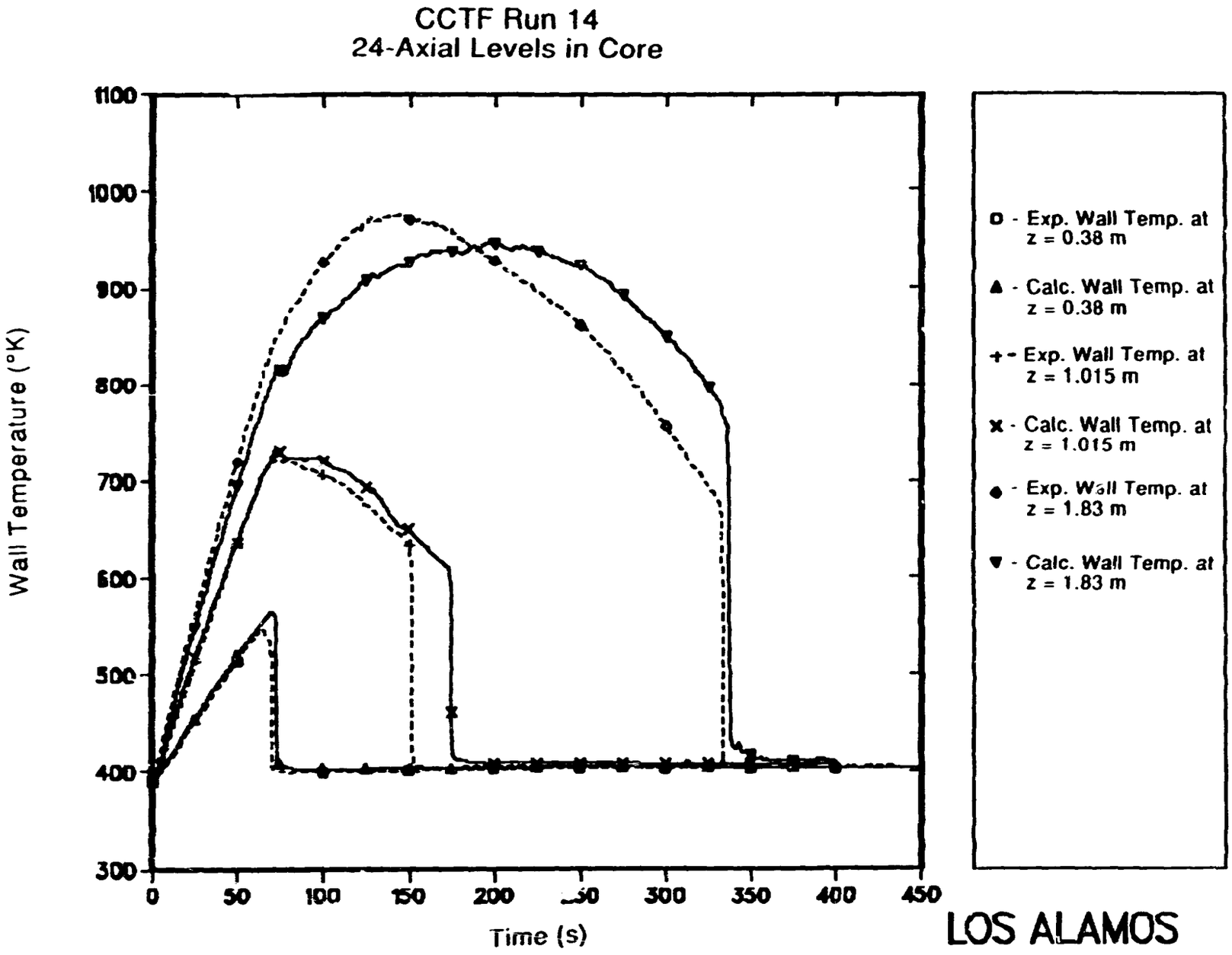

Fig. 17.
The predicted and measured wall temperature histories at the 0.38 m, 1.015 m, and 1.83 m elevations for the CCTF Run 14 test.